Journal of Molecular Liquids xxx (2020) xxx

Contents lists available at ScienceDirect

Journal of Molecular Liquids

journal homepage: www.elsevier.com/locate/molliq

Graphene oxide nanocomposite with Co and Fe doped $LaCrO_3$ perovskite active under solar light irradiation for the enhanced degradation of crystal violet dye

Muhammad Aamir [a], Ismat Bibi [a,*], Sadia Ata [b], Farzana Majid [c], Shagufta Kamal [d], Norah Alwadai [e], Misbah Sultan [b], Shahid Iqbal [a], Muhammad Aadil [a], Munawar Iqbal [f,*]

[a] Department of Chemistry, the Islamia University of Bahawalpur, Bahawalpur, Pakistan
[b] Institute of Chemistry, University of the Punjab, Lahore, Pakistan
[c] Department of Physics, University of the Punjab, Lahore, Pakistan
[d] Department of Applied Chemistry and Biochemistry, GC University, Faisalabad, Pakistan
[e] Department of Physics, College of Sciences, Princess Nourah bint Abdulrahman University (PNU), Riyadh 11671, Saudi Arabia
[f] Department of Chemistry, The University of Lahore, Lahore, Pakistan

ARTICLE INFO

Article history:
Received 4 September 2020
Received in revised form 9 November 2020
Accepted 25 November 2020
Available online xxxx

Keywords:
Perovskite nanoparticles
Graphene oxide
Micro-emulsion
Ultra-sonication
Electrical-conductivity
Crystal violet
Photocatalyst

ABSTRACT

Pristine $LaCrO_3$ and Co, Fe co-doped $La_{1-x}Co_xCr_{1-y}Fe_yO_3$ (x, y = 0.24) perovskite nanoparticles was prepared via micro-emulsion method and the $La_{1-x}Co_xCr_{1-}yFeyO_3$ composite was prepared with 5% reduced-graphene oxide (r-GO) by ultra-sonication process. The morphological, structural and thermal properties were investigated by Scanning Electron Microscopy (SEM), X-ray Diffraction (XRD), Raman Spectroscopy, Thermogravimetric Analysis (TGA) and Fourier Transform Infrared Spectroscopy (FTIR) techniques. The effect of Co, Fe doping and r-GO on the conductivity of the synthesized samples was investigated by current-voltage (I-*V*) analysis. The perovskite structure was orthorhombic with particle size in 21.24 to 31.58 nm range. Crystal violet (CV) dye was selected for evaluation of photocatalytic activity (PCA) of the prepared materials under visible light irradiation. $La_{1-x}Co_xCr_{1-y}Fe_yO_3$/r-GO showed remarkably higher PCA as compared to pristine $LaCrO_3$ and $La_{1-x}Co_xCr_{1-y}Fe_yO_3$. The r-GO composite furnished the CV dye degradation of 89.08% within 100 min irradiation under visible light at the light intensity in the range of 864.45–872.86 W/m^2. This valuable enhancement in PCA was due to the structural features of $La_{1-x}Co_xCr_{1-y}Fe_yO_3$/r-GO nanocomposite. In view of promising PCA, the composite has potential for the catalytic degradation of dyes in effluents using sunlight irradiation.

1. Introduction

Nanotechnology deals with the fabrication of material at the nanoscale that extends from 1 to 100 nm. The material having a size dimension in the nano-range exhibited ideal physicochemical properties as compared to bulk [1,2]. Nanomaterials gained much attention due to applications in diverse fields, i.e., medicine, agriculture, biotechnology, transportation, food industry, national defense, information technology, sensors, aerospace, packaging, textile, electronics and cosmetics [3–7]. Perovskite have general formula ABO_3 type, are very useful materials due to their unique structure and properties such as electric conductivity, dielectric, ferroelectric, anti-ferromagnetism, magnetic, thermochemical, and catalytic. Furthermore, these characteristic properties can be easily handled through the specific ratio of rare-earth ion A and B (transition metal ion) in the perovskite oxides [8,9]. The substitution of rare-earth ions with other rare-earth ion is the best way to enhance the functional properties, which play a vital role to fabricate many new-generation devices [10,11]. ABO_3 type mixed oxide perovskite nanomaterial such as $LaCrO_3$ [12], $NiTiO_3$, $BaZrO_3$, $CoTiO_3$, $LaMnO_3$, $LaNiO_3$, $PbTiO_3$ and $LaFeO_3$ [13] have been prepared using range of methods with the aim of application in different fields and promising efficiency have been documented. $LaCrO_3$-based perovskite oxides have been potentially used in SOFCs as a ceramic interconnecting material because of their high thermal, electrical and good phase stability under both reducing and air atmosphere [14] and due to its high catalytic activity, it is also used in catalytic combustion of methane [15].

In recent years, ABO_3 type perovskite oxides have been extensively used in heterogeneous catalysis because of their unique electronic properties [16]. However, one of main limitation of $LaCrO_3$ is less specific surface area, which cause a high deactivation based on the thermal sintering impact. The $LaCrO_3$ with higher surface area have efficient performance in catalytic applications. The surface area and conductivity of the $LaCrO_3$ can be accelerated by substituting the divalent metal ions in

* Corresponding author.
E-mail addresses: drismat@iub.edu.pk (I. Bibi), bosalvee@yahoo.com (M. Iqbal).

https://doi.org/10.1016/j.molliq.2020.114895
0167-7322/

the ABO3 lattice. The Cr^{3+} ion sites on the surface of pristine $LaCrO_3$ creates excellent adsorption conditions for atomic oxygen that blessed it with more suitable and favorable characteristics toward best photocatalytic applications under UV and visible light irradiation [8,9]. Recently, the foreign metal ions doping in the structure of NPs is a very useful way to enhance the conductivity and PCA of the doped nanomaterials [8,17,18]. Therefore, an attempt has been made to prepare the materials for PCA with large improved surface area and chemical stability with higher electron transportation capacity [1,2,19].

The rapid increase in population and industrialization affected the quality of the environment. Excessive contamination of water bodies with highly stable organic pollutants could be a serious threat to the living organisms. The dyes are one of toxic pollutants that are discharged into the wastewater resources from the textile, food, printing, and leather industries [20–22]. The existence of organic dyes contaminants in wastewater cause several severe health problems, inhibition in photosynthetic activity and put adverse effects on all types of aquatic life by blocking the sunlight and disturbing the dissolved oxygen of water [23,24]. Therefore, the degradation of organic dyes in wastewater demands advanced treatment methods due to their extremely slow biodegradation and toxic nature. Photocatalytic based advanced technique are efficient in the regard, which degrades the organic pollutants non-selectively and converts the toxic pollutants in to end-products (harmless) like CO_2 and H_2O along with inorganic ions [1,2,25]. In comparison to conventional methods for the treatment of wastewater [26–37], the advanced oxidation process is highly efficient, which remove the pollutants complete in water and wastewater by utilizing hydroxyl radicals [1,2,25,38,39].

Based on above mentioned facts, the pristine $LaCrO_3$, doped $La_{1-x}Co_xCr_{1-y}Fe_yO_3$ perovskite-nanoparticles and $La_{1-x}Co_xCr_{1-y}Fe_yO_3$/r-GO nanocomposite were prepared by micro-emulsion and ultra-sonication routes and characterized by TGA, XRD, FT-IR, SEM, raman-spectroscopy, EDX and UV–visible techniques. The PCA (under sunlight irradiation) of $La_{1-x}Co_xCr_{1-y}Fe_yO_3$ and $La_{1-x}Co_xCr_{1-y}Fe_yO_3$/r-GO nanocomposite was compared with pristine $LaCrO_3$.

2. Material and methods

2.1. Reagents and chemicals

The reagents and chemicals, i.e., lanthanum (III) nitrate hexahydrate (≥ 99%), cobalt(III) nitrate hexahydrate (≥ 98%), chromium (III) nitrate (≥ 98%), iron(III) nitrate (≥ 98%) were supplied by Sigma Aldrich (US). The CTAB (cetyltrimethylammonium bromide) was purchased from Bio basic Canada, INC.

2.2. Synthesis of $La_{1-x}Co_xCr_{1-y}Fe_yO_3$

$LaCrO_3$ and $La_{1-x}Co_xCr_{1-y}Fe_yO_3$ were fabricated via the micro-emulsion approach. Briefly, to synthesize pristine $LaCrO_3$ NPs the solution of La $(NO_3)_3.6H_2O$ and $Cr(NO_3)_3.9H_2O$ was prepared in 100 mL deionized water by dissolving stoichiometric ratio, 4.33 g, and 4.00 g respectively. Similarly, for the synthesis of $La_{1-x}Co_xCr_{1-y}Fe_yO_3$ NPs, 3.29 g of $La(NO_3)_3.6H_2O$, 0.70 g of $Co(NO_3)_2.6H_2O$, 3.04 g of $Cr(NO_3)_3.9H_2O$ and 0.96 g of $Fe(NO_3)_3.9H_2O$ were dissolved in 76 mL, 24 mL, 76 mL, and 2 mL deionized water, respectively. After solution preparation, sample solutions were mixed and put on the hotplates keeping stirring and heating on. When the temperature of the sample solutions reaches 50 °C, 100 mL (0.3 M) CTAB solution was added to both sample solutions. After the successful addition of the CTAB solution, the heating process was closed and then, 10 mL (0.3 M) NH_4OH aqueous solution was added to sample solutions after a constant interval of time (10 min) till 2 h with continuous stirring. After the successful addition of (0.3 M) NH_4OH, sample solutions were subjected to continuous stirring till 5 h, and nanoparticles have been appeared in this step. Then washing of these nanoparticles was done via deionized water several times to lower down pH up to 7. After washing particles were dried completely in an oven at 100 °C and then dried particles were grounded and calcined at 900 °C for 7 h. The systematic scheme for the synthesis of $LaCrO_3$ and $La_{1-x}Co_xCr_{1-y}Fe_yO_3$ nanoparticles is shown in Fig. 1.

2.3. Preparation of GO

The GO (graphene oxide) suspension was synthesized following Hummer's method using graphite powder. In this process, conc. H_2SO_4 (75 mL), $NaNO_3$ (2 g), and graphite powder (2 g) were mixed in a 200 mL for 40 min on a magnetic stirrer. The resulting combination was kept in ice-bath and then, 10 g $KMnO_4$ salt was propped with continuous stirring. During this addition, the temperature of the mixture was 18 °C. The obtained slurry was further stirred on a magnetic stirrer for two days. Then, the mixture was diluted with pure water a greenish-black was appeared and its temperature increases up to 80 °C and when temperature reached to 30 °C, H_2O_2 (33%) was added that resulted in a brilliant yellowish mixture. Then resulting yellowish mixture was subjected to washing several times by HCl and H_2O_2 mixture and later with pure water until the pH reached 7. Finally, the drying was done at 25 °C and then, it was dispersed in deionized water to get the GO [40].

2.4. Synthesis of r-GO

The GO was reduced chemically using liquid ammonia as exfoliating and hydrazine as a reducing agent. Firstly, the GO was diluted with water and it was sonicated for 3 h, and heating was done in a paraffin oil bath up to 80 °C and added liquid ammonia and hydrazine in it. Finally, the mixture was heated and stirred until the greyish suspension of r-GO was obtained [41]. A systematic scheme for the synthesis of GO and its reduction into a r-GO is shown in step II of Fig. 1.

2.5. Synthesis of $La_{1-x}Co_xCr_{1-y}Fe_yO_3$/r-GO composite

The $La_{1-x}Co_xCr_{1-y}Fe_yO_3$/r-GO composite was synthesized by the ultra-sonication method. The $La_{1-x}Co_xCr_{1-y}Fe_yO_3$ (76 mg) was mixed in 100 mL of r-GO aqueous solution (40 mg/L) and then, the resulting material was sonicated for 50 min to obtain the highly dispersed mixture and drying was done at 90 °C for 2 h to obtain the required $La_{1-x}Co_xCr_{1-y}Fe_yO_3$/r-GO nanocomposite [42]. A systematic scheme for the fabrication of $La_{1-x}Co_xCr_{1-y}Fe_yO_3$/r-GO nanocomposite is shown in step III of Fig. 1.

2.6. Characterization

The $LaCrO_3$ NPs, $La_{1-x}Co_xCr_{1-y}Fe_yO_3$ NPs and $La_{1-x}Co_xCr_{1-y}Fe_yO_3$-r-GO nanocomposite were investigated by XRD analysis using X-ray Diffractometer (Phillips, X- pert PRO 3040/60), having CuKα as a source of radiation with $\lambda = 1.542$ Å in 2θ range of 20°-80°). For morphological study, S-3400 SEM was employed. The Yyon Atago/Bussan spectrometer (Via T- 6400 Triple-Jobin,) was employed for Raman spectra recording (in the range of 100 cm^{-1} to 800 cm^{-1}) were recorded. The FTIR (Tensor-27) was employed to investigate the functionalities in the $La_{1-x}Co_xCr_{1-y}Fe_yO_3$ NPs and $La_{1-x}Co_xCr_{1-y}Fe_yO_3$-r-GO nanocomposite. Furthermore, two probes current-voltage (I-V) investigations, was done by Keithley-487 Picoammeter and a UV- visible spectrum was recorded using Dual-beam Cary 60 spectrophotometer.

2.7. Photocatalytic activity

The PCA of the synthesized samples ($LaCrO_3$ NPs, $La_{1-x}Co_xCr_{1-y}Fe_yO_3$ NPs and $La_{1-x}Co_xCr_{1-y}Fe_yO_3$-r-GO nanocomposite) was studied through CV dye degradation under sunlight (Time: 11:00 am to 12:30 pm, dated: 13-July 2020, Place: Bahawalpur, Pakistan). The intensity of

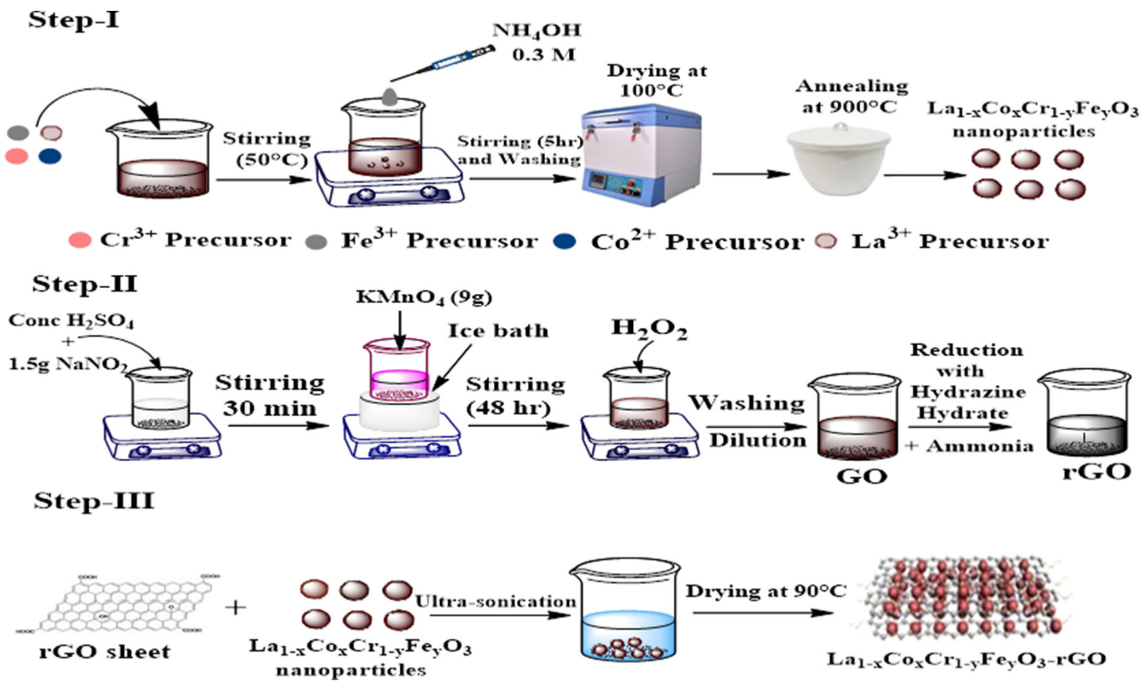

Fig. 1. Schematic flow sheet diagram for the formation of $La_{1-x}Co_xCr_{1-y}Fe_yO_3$ NPs (Step 1), r-GO (Step II), and their nanocomposite (Step III).

sunlight radiations was measured by Kipp & Zonen CMP-11 pyranometer and it was found in the range of 864.45–872.86 W/m^2. A 5 mg of $LaCrO_3$, $La_{1-x}Co_xCr_{1-y}Fe_yO_3$ and $La_{1-x}Co_xCr_{1-y}Fe_yO_3$-r-GO nanocomposite was mixed with 5 ppm CV dye solution (50 mL) and mixture was subjected to continuous stirring for 30 min in dark and concentration of CV dye was noted before and after dark-reaction to determine the of dye adsorbed and for the concentration determination of the dye, 4 mL sample was taken at a specific time interval (15 min). After that, the catalyst was separated by the centrifugation process, and then obtained supernatant was further subjected to find out the absorption spectra of the CV dye at 672 nm. The CV dye degradation (%) was computed by Eq. (1) [42,43].

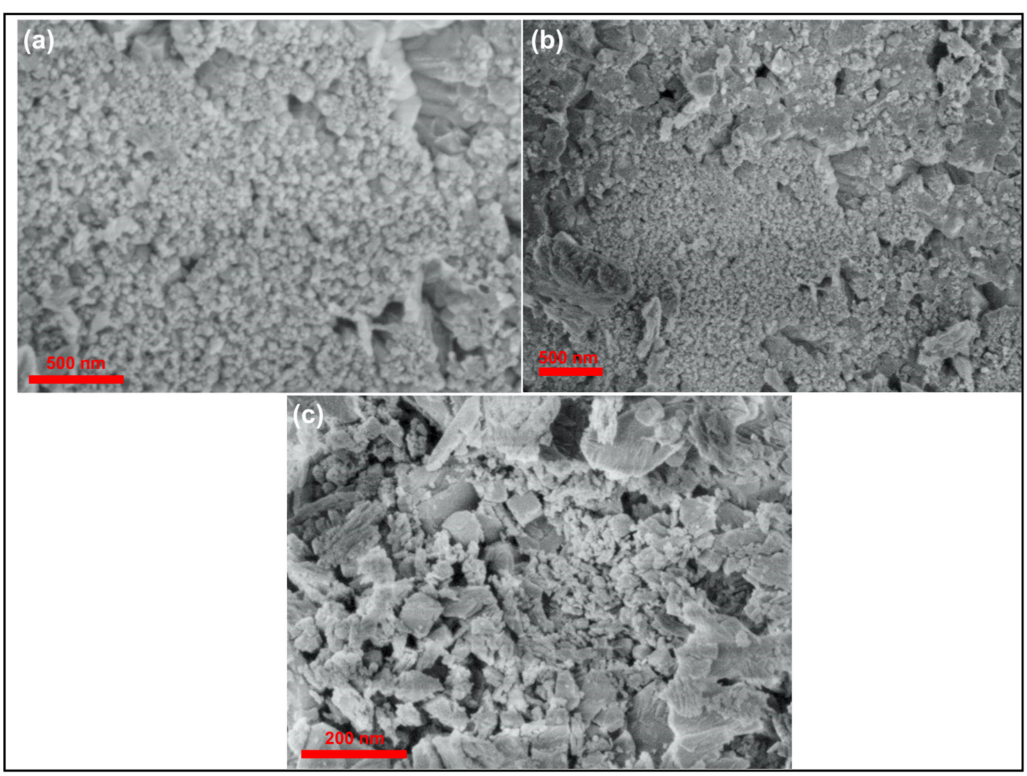

Fig. 2. SEM images, (a) pristine $LaCrO_3$ NPs, (b) doped $La_{1-x}Co_xCr_{1-y}Fe_yO_3$ NPs and (c) $La_{1-x}Co_xCr_{1-y}Fe_yO_3$/r-GO nanocomposite.

$$\text{Degradation}\ (\%) = 1 - \frac{C_t}{C_0} \quad (1)$$

where, C_0, and C_t are depicting the absorbance values of initial and dye concentration at time "t", respectively [44].

3. Results and discussion

3.1. Surface morphology

The morphological investigation of the $LaCrO_3$, $La_{1-x}Co_xCr_{1-y}Fe_yO_3$ and $La_{1-x}Co_xCr_{1-y}Fe_yO_3$/r-GO nanocomposite were done using SEM and responses, thus observed are depicted in Fig. 2. The pristine $LaCrO_3$ NPs show heterogeneous morphology with particle size range 82–87 nm as shown in Fig. 2a. While the SEM image of doped $La_{1-x}Co_xCr_{1-y}Fe_yO_3$ nanoparticles (Fig. 2b) shows that the particles are fused and formed agglomerates and it is noticed that, the particle size decreases with doping and resultantly, agglomeration phenomenon among particles was observed [45]. The average particle size of the doped $La_{1-x}Co_xCr_{1-y}Fe_yO_3$ NPs was determined from the well-scattered zones and it was 78.4 nm. While in the case of $La_{1-x}Co_xCr_{1-y}Fe_yO_3$/r-GO nanocomposite (Fig. 2c), the particles are finely mixed with r-GO and their agglomeration reduced slightly. The r-GO nano sheets due to its excellent 2D nanostructure feature, it provides sufficient surfaces for the loading of nanoparticles.

3.2. Composition analysis

Fig. 3a, b, and c, shows the spectra of $LaCrO_3$, doped $La_{1-x}Co_xCr_{1-y}Fe_yO_3$ and $La_{1-x}Co_xCr_{1-y}Fe_yO_3$/r-GO nanocomposite, respectively for EDX investigation. The EDX spectra of $LaCrO_3$ (Fig. 3a) clearly show the existence of very fine peaks of La, Cr, and O. Similarly, The EDX spectra of doped $La_{1-x}Co_xCr_{1-y}Fe_yO_3$ and $La_{1-x}Co_xCr_{1-y}Fe_yO_3$/r-GO nanocomposite (Fig. 3b and c) also shows the clear characteristic peaks of La, Co, Cr, Fe, O and La, Co, Cr, Fe, C and O. Hence, the absence of any other impurity/contamination peaks in all three EDX spectra has confirmed the purity and successful synthesis of the desired materials.

3.3. Structural analysis

The XRD responses of $LaCrO_3$, $La_{1-x}Co_xCr_{1-y}Fe_yO_3$ and $La_{1-x}Co_xCr_{1-y}Fe_yO_3$-r-GO nanocomposite is shown in Fig. 4a. The crystal structure conformation was determined by taking XRD in 2θ range of 20 to 80°. From the XRD data, it was noticed that the diffraction peaks of fabricated nanoparticles appeared at 21.72°, 31.35°, 39.01°, 45.65°, 51.76°, 57.09°, 67.01°, 76.72°, which correspond to the miller indices values; (110), (112), (022), (004), (114), (024), (224), (314), (044), respectively. The diffraction patterns of $La_{1-x}Co_xCr_{1-y}Fe_yO_3$ nanoparticles reflects pure perovskite phase and matched with JCPDS # 024–1016, all peaks correspond to an orthorhombic structure with space group Pbnm without any contaminated phase [46]. Lattice constants values were determined by 'cell software' and particle size was determined with the help of Debye Scherrer equation Eq. (2). [47].

$$D = \frac{0.9\,\lambda}{\beta cos\theta} \quad (2)$$

where, 'D' is the average size for the particles, while 'λ' expresses the wavelength (1.542 Å) of X-rays used. The 'β' represents the full-width at half maxima while 'θ' expresses the Bragg's angle and 0.9 is the value of constant K. The calculated crystallite size of $La_{1-x}Co_xCr_{1-y}Fe_yO_3$ by the Scherrer equation was found to be 21.24 nm to 31.58 nm. Unit cell volume for the orthorhombic system was computed as per Eq. (3) [48]. The X-ray density was measured using Eq. (4) [41].

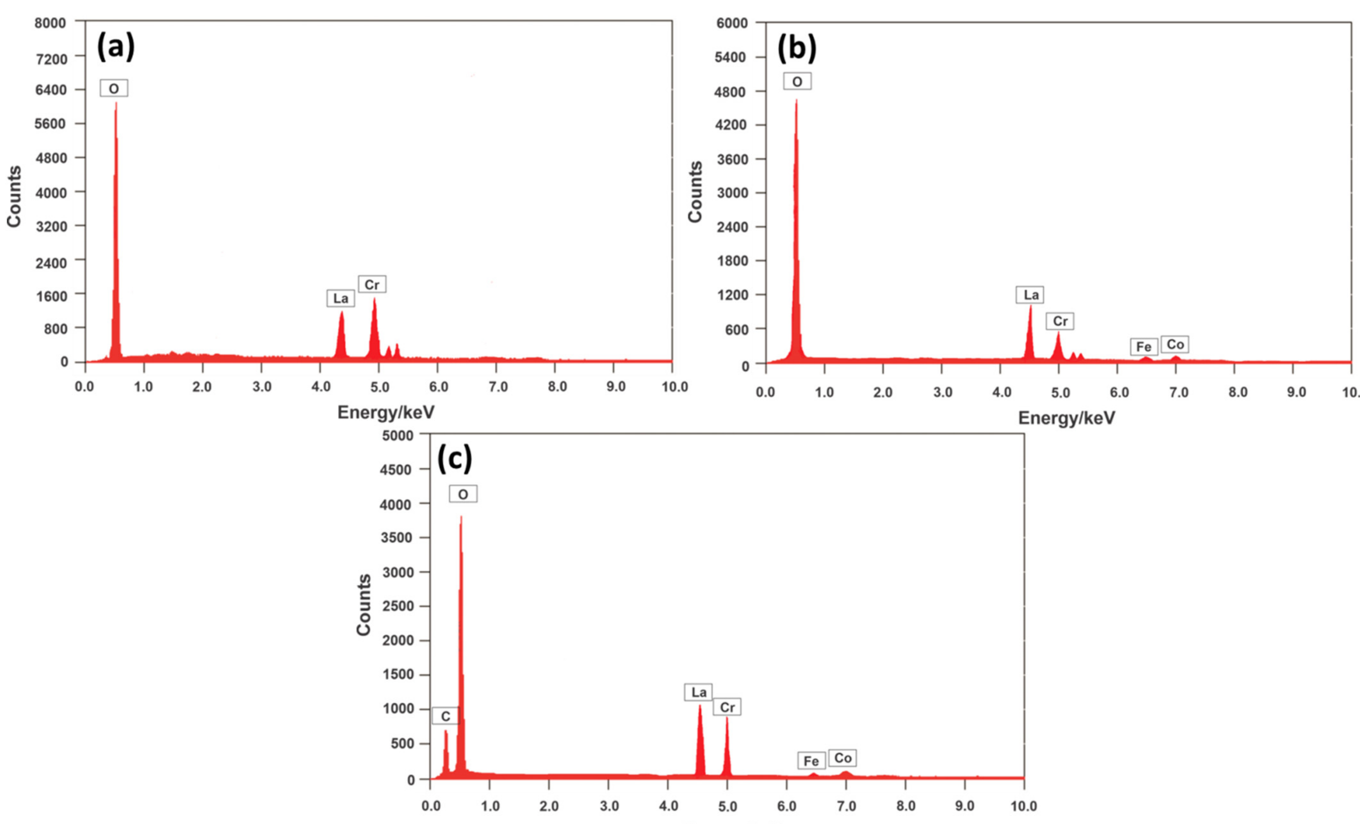

Fig. 3. EDX spectra, (a) pristine $LaCrO_3$ NPs, (b) doped $La_{1-x}Co_xCr_{1-y}Fe_yO_3$ NPs and (c) $La_{1-x}Co_xCr_{1-y}Fe_yO_3$/r-GO nanocomposite.

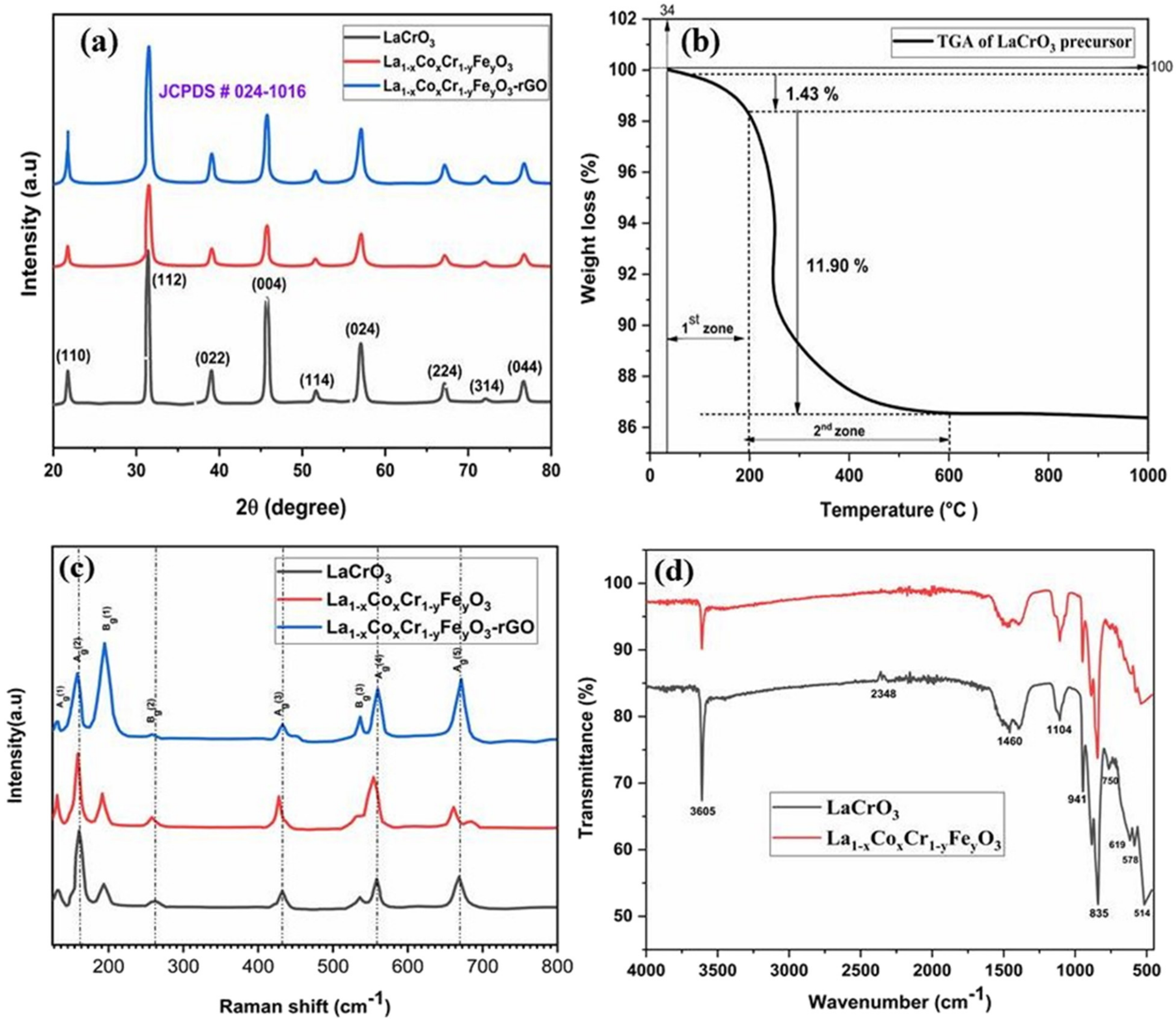

Fig. 4. (a) XRD pattern of fabricated NPs, (b) TGA curve of pristine $LaCrO_3$ NPs, (c) Raman spectra, (d) FTIR spectra of pristine $LaCrO_3$ and doped $La_{1-x}Co_xCr_{1-y}Fe_yO_3$ NPs.

$$\text{Cell volume} = a \times b \times c \tag{3}$$

$$\rho_{x-ray} = \frac{z.M_w}{N_{A.}V} \tag{4}$$

where, 'z' represents the number of atoms per unit cell, M_w expresses the MW, N_A represents the Avogadro's number and V expresses the volume of the unit cell. The obtained value of X-ray density for pristine $LaCrO_3$ was 6.35 g/cm^3. From the above calculations it was concluded that as we increase the x and y concentrations, the crystalline size of fabricated nanoparticles also increases from 21.24 nm to 31.58 nm, this increase in crystalline size by doping may be due to the larger ionic radii of Co^{3+} ion (0.72 Å), Fe^{3+} ion (0.64 Å) against the ionic radii of Cr^{3+} ion (0.62 Å), which confirmed the successful substitution of Cr and Fe [49–53]. The cell volume of $La_{1-x}Co_xCr_{1-y}Fe_yO_3$ perovskite nanoparticles was decreased by increasing Co^{3+} and Fe^{3+}ions concentration. This decrease in cell volume is because of the smaller ionic radii of Co^{3+} (0.72 Å) ion as compare to the La^{3+} (1.03 Å) ion which also proved that successful substitution of La and Co [54–56]. The bulk density (ρ_{bulk}) was also determined using Eq. (5) [57].

$$\rho_{Bulk} = \frac{m}{v} \tag{5}$$

where 'm' represents the mass of the pellet and 'v' express the volume of the pellet. With the help of these two densities, the percentage of porosity (P) was calculated using Eq. (6) [58].

$$Porosity = \frac{1-\rho_{Bulk}}{\rho_{x-ray}} \times 100 \tag{6}$$

The percentage of porosity value of synthesized nanoparticles was recorded in 42.04 to 51.81 nm range and a comparison among the crystallographic parameter of pristine and doped samples is given in Table 1.

Table 1
Cell parameters, cell volume, crystallite size, X-ray density, bulk density and porosity for pristine $LaCrO_3$, $La_{1-x}Co_xCr_{1-y}Fe_yO_3$ and $La_{1-x}Co_xCr_{1-y}Fe_yO_3$/r-GO nanocomposite.

Par parameters	Pristine $LaCrO_3$0.0.0	Doped $La_{1-x}Co_xCr_{1-y}Fe_yO_3$
Lattice-constant a/A°	5.558	5.764
Lattice-constant b/A°	6.267	5.565
Lattice-constant c/A°	8.000	7.883
Cell volume / A$^{3°}$	278.65	252.86
Crystallite size/nm	21.24	31.58
X-ray density/gcm^{-3}	5.60	6.17
Bulk density/gcm^{-3}	3.047	2.993
Porosity (%) P (a.u)	45.58	51.49

3.4. Thermogravimetric analysis (TGA)

The thermal transformation of the pristine $LaCrO_3$ was done through TGA. The obtained thermo-gram of the pristine $LaCrO_3$ is shown in Fig. 4b. According to a thermo-gram, weight loss takes place between two temperature zones. The weight loss in the first temperature zone was noticed between 34 and 200 °C, and in this zone, 1.43% weight loss was investigated, which is may be a result of the desorption of water contents. While the second temperature zone was noticed between 200 and 600 °C and in this zone 11.90% weight loss takes place, which might be due the formation of lanthanum oxide from Lanthanum hydroxide breakdown with hydroxide and lanthanum oxide as an intermediate product. The weight losses in both zones are expressed by the Eqs. (7)–(8), respectively [59]. The observed weight loss (11.90%) which is the result of decomposition of the precursors is closed to the theoretically determined weight loss (13.67%). The creation of $LaCrO_3$ using lanthanum and chromium oxide can be expressed in Eqs. (9)–(10).

$$La(OH)_3\ (s) + heat \rightarrow LaO(OH)\ (s) + H_2O\ (g) \tag{7}$$

$$2LaO(OH)\ (s) + heat \rightarrow La_2O_3\ (s) + H_2O\ (g) \tag{8}$$

$$6Cr(OH)_3\ (s) + 1/2\ O_2\ (g) + heat \rightarrow 2Cr_3O_4\ (s) + 9H_2O\ (l) \tag{9}$$

$$3La_2O_3\ (s) + 2Cr_3O_4\ (s) + 1/2O_2\ (g) + heat \rightarrow 6LaCrO_3\ (s) \tag{10}$$

3.5. Raman scattering

Raman spectrum of pristine $LaCrO_3$, $La_{1\text{-}x}Co_xCr_{1\text{-}y}Fe_yO_3$ and $La_{1\text{-}x}\ Co_xCr_{1\text{-}y}Fe_yO_3$/r-GO nanocomposite was noted in 100 to 800 cm^{-1} range at ambient temperature and obtained peaks were assigned to various Raman modes as shown in Fig. 4c. Out of 8 Raman modes, in the current study, 5 modes were found at 132, 158, 432, 560, and 672 cm^{-1} that are assigned to A_g symmetry, while other modes 195, 258, 536 cm^{-1} belong to B_g symmetry. The bands noticed at $A_g(1)$, $A_g(2)$ and $B_g(1)$ attributed to rare-earth ions because of the greater atomic mass of R^{3+} ions also known as vibrational modes. The $A_g(5)$ mode allied with the tilting of CrO_6 octahedral and it shifted toward the high wavenumber region, which has been attributed to an rise in the tilt of CrO_6 octahedral due to reduction of R^{3+} radii. The modes $B_g(2)$ and $B_g(3)$, which are due to the CrO_6 octahedral (bending and rotation) and shifting toward high wavenumber, which reveals distortion in the orthorhombic structure. The fluctuation toward high wavenumber are the result of anti-symmetric stretching vibrations of O-Cr-O and this shifting also fluctuates as the R^{3+} ionic radii changes [46,60]. Moreover, no inferior peak was found in the spectra which confirmed the structure of fabricated nanoparticles in a single phase and the width of the bands attributed to the grain-size of the fabricated NPs [61].

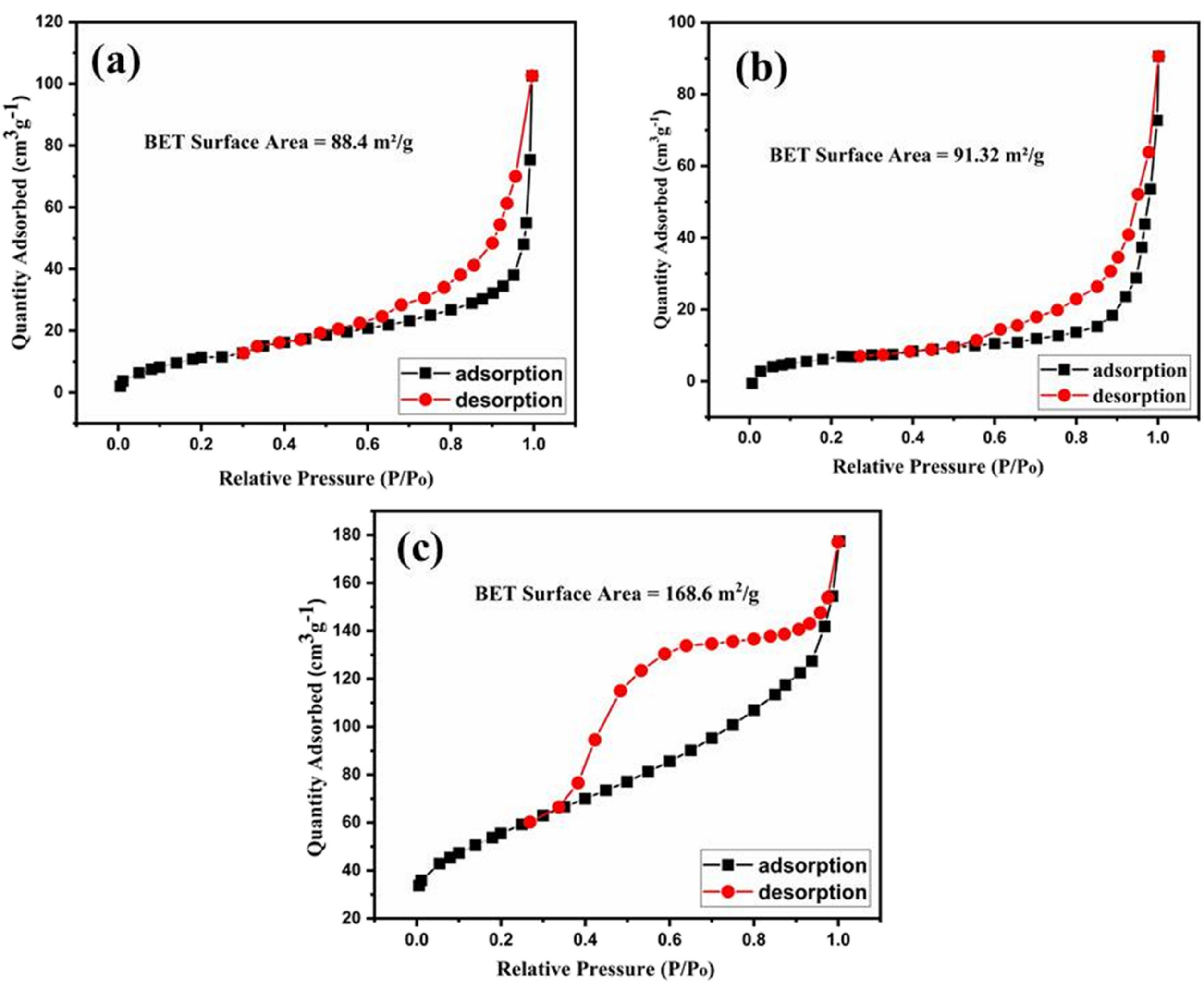

Fig. 5. Nitrogen physisorption isotherms, (a) pristine $LaCrO_3$, (b) $La_{1\text{-}x}Co_xCr_{1\text{-}y}Fe_yO_3$ NPs (c) $La_{1\text{-}x}Co_xCr_{1\text{-}y}Fe_yO_3$/r-GO nanocomposite.

3.6. FT-IR analysis

The functional group was studied by FTIR analysis in 400 to 4000 cm^{-1} range and outcomes, thus observed are depicted in Fig. 4d. A two intense bands in 400 cm^{-1} to 850 cm^{-1} range was observed, which was due to the Cr—O stretching and O—Cr—O deformation, respectively. The band detected at 941 cm^{-1}, reveals the stretching of La—O, Co—O and Fe—O bonds, another feature by the increasing of x and y concentration slightly shift in the metal-oxygen stretching peak was noticed from 835 cm^{-1} to 1104 cm^{-1}. This shift may be due to the increasing bond strength and decreasing ionic radii by the doping Co element. The bands observed between 1100 cm^{-1} to 1500 cm^{-1} may be attributed to the distortion in water molecules. The large peak detected at 3605 cm^{-1} indicates stretching of O—H for an adsorbed water molecule, which is in the agreement with reported studied [62–65].

3.7. BET analysis

The BET technique was employed to investigate the surface area of the fabricated samples. The N_2 adsorption-desorption isotherm curves of the $LaCrO_3$, $La_{1-x}Co_xCr_{1-y}Fe_yO_3$ and $La_{1-x}Co_xCr_{1-y}Fe_yO_3$/r-GO nanocomposite are depected in Fig. 5. The BET surface area of the $LaCrO_3$ (Fig. 5a), $La_{1-x}Co_xCr_{1-y}Fe_yO_3$ (Fig. 5b), and $La_{1-x}Co_xCr_{1-y}Fe_yO_3$/r-GO nanocomposite (Fig. 5c) were 88.4 m^2/g, 91.32 m^2/g and 168.6 m^2/g, respectively. The observed BET surface area of $La_{1-x}Co_xCr_{1-y}Fe_yO_3$/r-GO nanocomposite (168.6 m^2/g) was larger than the pristine $LaCrO_3$ NPs (88.4 m^2/g) and doped $La_{1-x}Co_xCr_{1-y}Fe_yO_3$ (91.32 m^2/g). The BET specific surface area of pristine $LaCrO_3$ (88.4 m^2/g) and doped $La_{1-x}Co_xCr_{1-y}Fe_yO_3$ (91.32 m^2/g) are comparatively close to each other, but less than the BET surface area of $La_{1-x}Co_xCr_{1-y}Fe_yO_3$/r-GO nanocomposite (168.6 m^2/g), which is due to their agglomeration and stacking effects. The higher BET surface area in the case of $La_{1-x}Co_xCr_{1-y}Fe_yO_3$/r-GO nanocomposite (168.6 m^2/g) can be described based on two facts. Firstly, the 2D r-GO sheets itself provided an additional surface to the $La_{1-x}Co_xCr_{1-y}Fe_yO_3$/r-GO nanocomposite. Secondly, the r-GO nano sheets act as volume buffering agents and preclude the NPs from agglomeration formation, which resultantly, enhanced the surface area.

3.8. Current-voltage (I-V) analysis

To study the effect of Co and Fe doping on the conductivity (σ), the doped $La_{1-x}Co_xCr_{1-y}Fe_yO_3$ and $La_{1-x}Co_xCr_{1-y}Fe_yO_3$/r-GO nanocomposite were tested via two-probe current-voltage measurements (I-*V*). For this measurement, samples pellets (3 mg) were prepared with

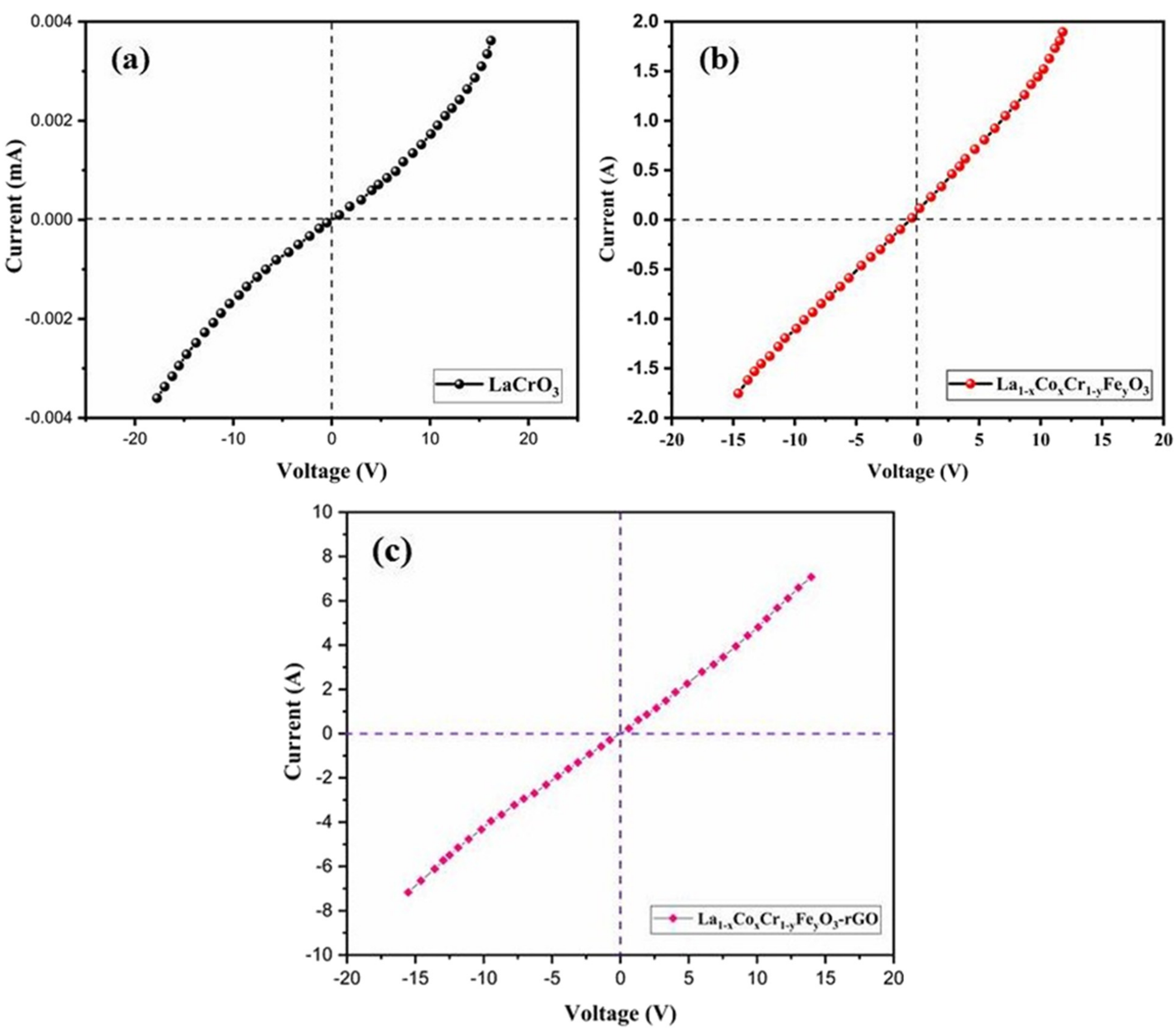

Fig. 6. I-V profiles of $LaCrO_3$, (b) $La_{1-x}Co_xCr_{1-y}Fe_yO_3$ NPs (c) $La_{1-x}Co_xCr_{1-y}Fe_yO_3$/r-GO nanocomposite.

2.27 mm (w) width and 7.85 mm (d) diameter. By using this, the area (A) of the pellets was calculated as depicted in Eq. (11) [66].

$$A = \pi\left(\frac{d}{2}\right)^2 \tag{11}$$

The I-V profiles of the $LaCrO_3$, $La_{1-x}Co_xCr_{1-y}Fe_yO_3$ and $La_{1-x}Co_xCr_{1-y}Fe_yO_3$/r-GO are shown in Fig. 6. The I-V curve of the $LaCrO_3$ (Fig. 6a) is non-linear that reflects its non-ohmic and semi-conductive behavior. While Co and Fe doped $LaCrO_3$ exhibits an almost linear I-V curve (Fig. 6b) with a better current-voltage response. Whereas, a straight I-V curve of $La_{1-x}Co_xCr_{1-y}Fe_yO_3$/r-GO nanocomposite with an excellent current-voltage output is shown in Fig. 6c. This excellent response is the result of two factors, r-GO addition and doping of Co and Fe ions. The electrical conductivity (σ) values for all prepared samples were determined using Eq. (12).

$$\sigma = \frac{w}{RA} \tag{12}$$

where, A, R, and w are the area, resistance and width of the pellets, respectively, the values of R (resistance) was determined from I-V curves using Ohm's equation (V = IR). The determined σ values of the $LaCrO_3$, doped $La_{1-x}Co_xCr_{1-y}Fe_yO_3$ and $La_{1-x}Co_xCr_{1-y}Fe_yO_3$/r-GO nanocomposite are 2.17×10^{-2} Sm^{-1}, 3.38×10^3 Sm^{-1} and 7.4×10^3 Sm^{-1}, respectively. The observed results indicate that the higher electrical conductivity (σ) value of the doped $La_{1-x}Co_xCr_{1-y}Fe_yO_3$ and $La_{1-x}Co_xCr_{1-y}Fe_yO_3$/r-GO nanocomposite that is referred to the reduction in the band gap, after r-GO addition and doping of Co, Fe ions. The UV–visible investigation also confirmed the successful reduction in band gap of $La_{1-x}Co_xCr_{1-y}Fe_yO_3$/r-GO nanocomposite that is due to r-GO addition and doping of Co and Fe ions [40,67].

3.9. Photocatalytic degradation of dye

The PCA of $LaCrO_3$, doped $La_{1-x}Co_xCr_{1-y}Fe_yO_3$ and $La_{1-x}Co_xCr_{1-y}Fe_yO_3$/r-GO nanocomposite was investigated by degrading the CV dye under visible light. The recorded UV–visible absorption spectra of the dye are shown in Fig. 7(a-c). The degradation efficiency of the pristine $LaCrO_3$, doped $La_{1-x}Co_xCr_{1-y}Fe_yO_3$ and $La_{1-x}Co_xCr_{1-y}Fe_yO_3$/r-GO nanocomposite are explained in term of C_t/C_0 as shown in Fig. 8a, where C_0 express the initial concentration of the CV dye and Ct, express the concentration at a specific time interval.

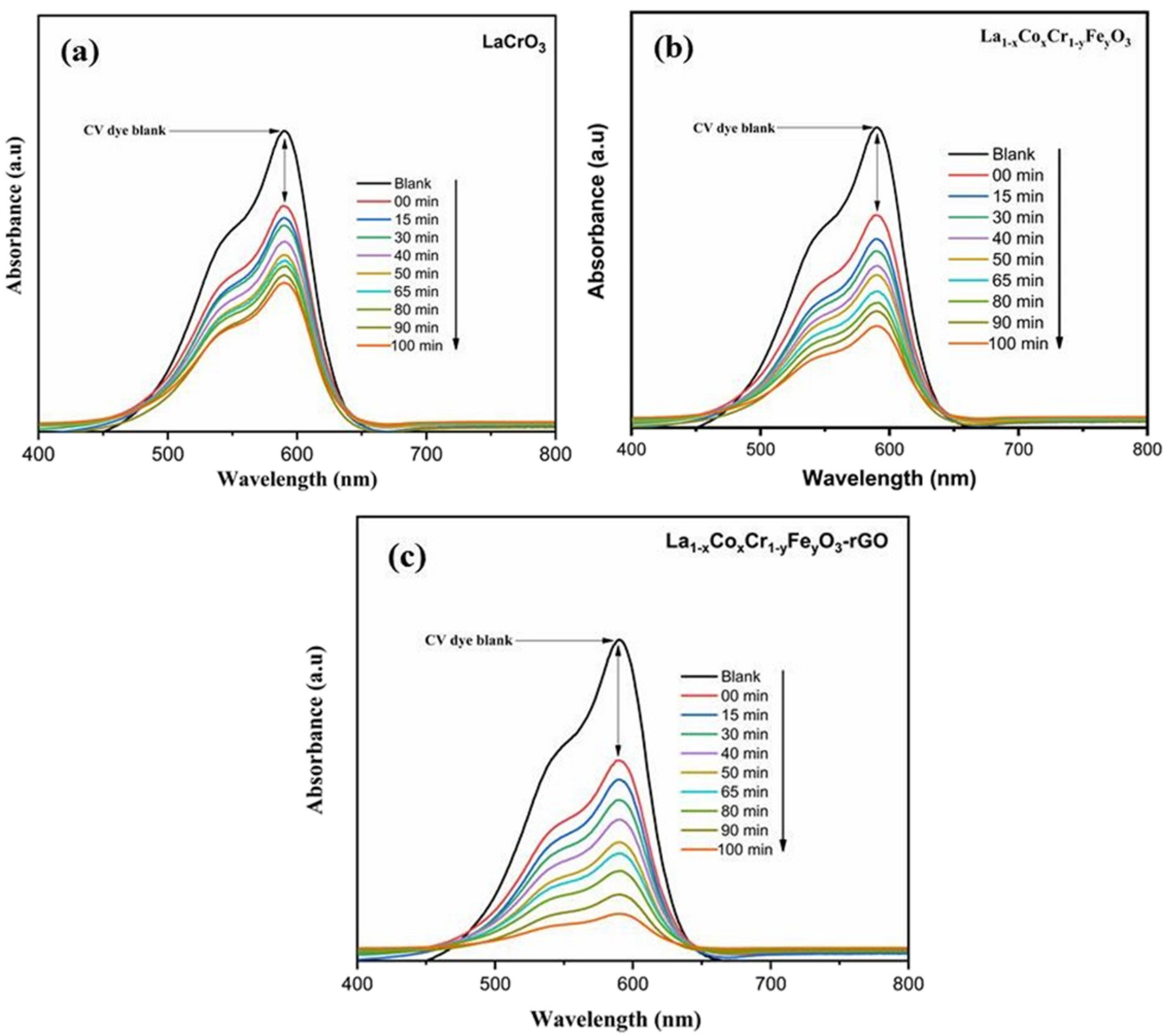

Fig. 7. Absorption spectra of CV dye photo-degradation over, (a) pristine $LaCrO_3$ (b) doped $La_{1-x}Co_xCr_{1-y}Fe_yO_3$ and (c) $La_{1-x}Co_xCr_{1-y}Fe_yO_3$/r-GO nanocomposite.

From the UV–visible profiles, it is clear that $La_{1-x}Co_xCr_{1-y}Fe_yO_3$/r-GO degrades the CV dye faster as compared to pristine $LaCrO_3$ and doped $La_{1-x}Co_xCr_{1-y}Fe_yO_3$ and the % degradation of CV dye was recorded to be 35.78, 55.27 and 89.08 (%) for pristine $LaCrO_3$, $La_{1-x}Co_xCr_{1-y}Fe_yO_3$ and $La_{1-x}Co_xCr_{1-y}Fe_yO_3$/r-GO, respectively (Fig. 8d). The high catalytic efficiency of the $La_{1-x}Co_xCr_{1-y}Fe_yO_3$ (55.27%) as compared to pristine $LaCrO_3$ (35.78%) is the result of defects that are generated by doping [68]. Moreover, the dopants act like trapping agents toward holes/electrons to retard their recombination phenomenon. While in the case of $La_{1-x}Co_xCr_{1-y}Fe_yO_3$/r-GO, the percentage of CV dye degradation was 89.08%. It is due to the r-GO nano sheets that shielded the $La_{1-x}Co_xCr_{1-y}Fe_yO_3$ agglomeration process and resultantly, surface to volume ratio increases. Hence, $La_{1-x}Co_xCr_{1-y}Fe_yO_3$/r-GO due to its larger surface area adsorbed a higher amount of CV dye and resultantly, it degraded 89.08% of CV dye, which is a promising catalytic efficiency [69]. The PCA of the $LaCrO_3$, $La_{1-x}Co_xCr_{1-y}Fe_yO_3$ and $La_{1-x}Co_xCr_{1-y}Fe_yO_3$/r-GO composite was studied through kinetics of the CV dye photodegradation, which followed the first-order kinetics [70].

$$-\ln Ct/C_0 = kt \tag{13}$$

where, C_0 and Ct are CV dye concentration at zero time and a specific interval of time, respectively. 'k' express the rate constant, while 't' express the reaction time. A straight line is obtained (Fig. 8b) by plot –ln Ct/C_o vs. t and the value of 'k' in min^{-1} can be calculated through the slope of the straight line [71]. The values of rate constant (k) (Fig. 8c) for the degradation of CV dye by pristine $LaCrO_3$, doped $La_{1-x}Co_xCr_{1-y}Fe_yO_3$ and $La_{1-x}Co_xCr_{1-y}Fe_yO_3$/r-GO are 0.00311 min^{-1}, 0.00845 min^{-1} and 0.0195 min^{-1}, respectively [72]. In-fact, faster degradation of CV dye with $La_{1-x}Co_xCr_{1-y}Fe_yO_3$/r-GO is mainly due to the existence of effective charge separation in the $La_{1-x}Co_xCr_{1-y}Fe_yO_3$/r-GO composite and it may also be due to the formation of heterojunction between the $La_{1-x}Co_xCr_{1-y}Fe_yO_3$ and r-GO. Moreover, the existence of the r-GO in $La_{1-x}Co_xCr_{1-y}Fe_yO_3$/r-GO nanocomposite not only provides a large surface area to facilitate the adsorption of CV dye, but also

Table 2
The comparison of the PCA of the $La_{1-x}Co_xCr_{1-y}Fe_yO_3$/r-GO (for CV dye) with reported similar studies.

Photo-catalysts	Dye	Degradation (%)	Time (min)	Reference
CdS/CMS	CV	81.03	120	[74]
Fe_3O_4/ZnO/CRC	CV	75	60	[75]
TiO_2(B)/fullerene	CV	82	300	[76]
Co_3O_4 NPs	CV	64	45	[77]
TiO_2/clinoptilolites	CV	89	100	[78]
FB-HAp	CV	77	75	[79]
S/RGO	CV	68	240	[80]
$La_{1-x}Co_xCr_{1-y}Fe_yO_3$/r-GO	CV	89.08	90	Present study

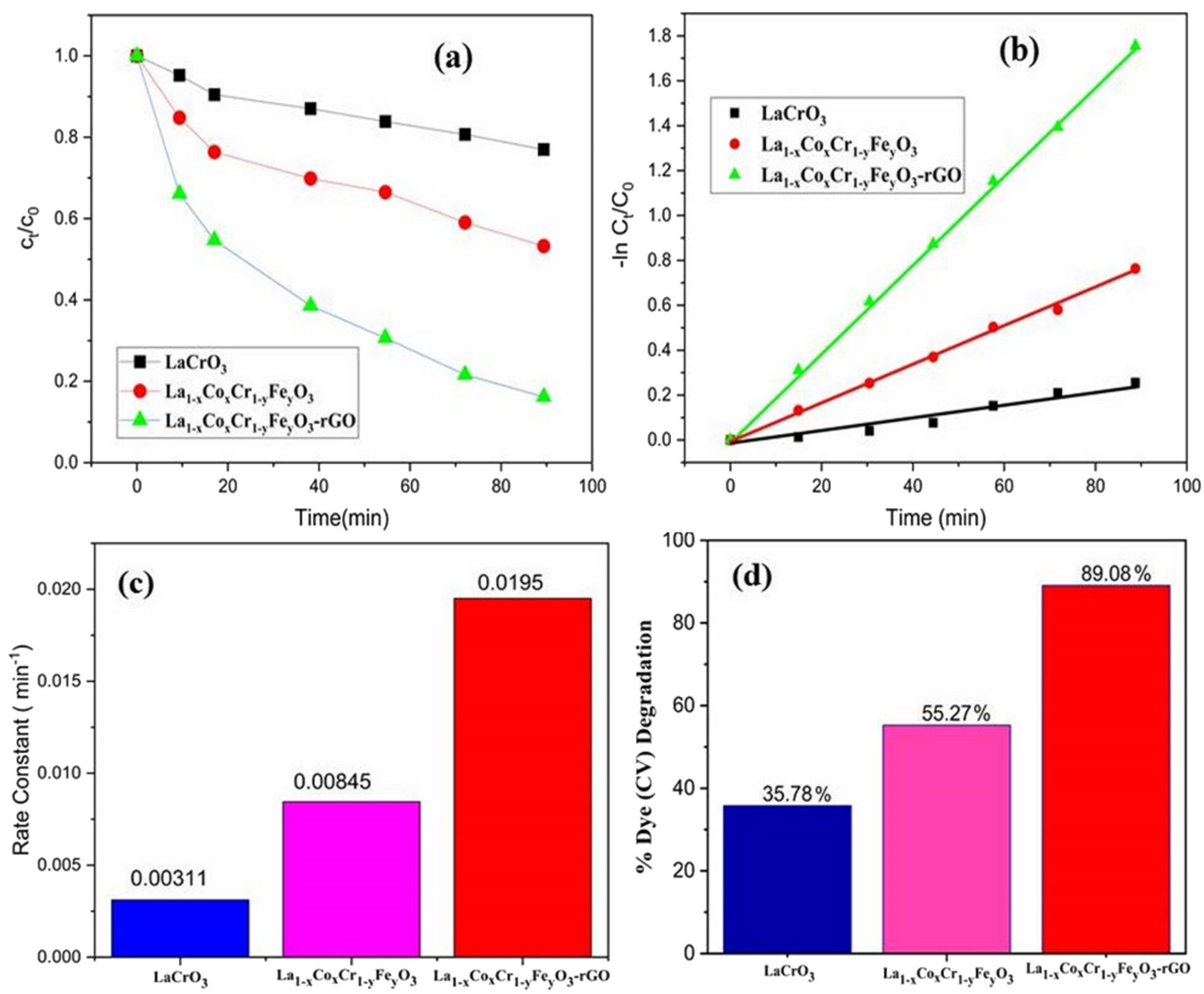

Fig. 8. Degradation curves profiles of CV dye over pristine $LaCrO_3$, $La_{1-x}Co_xCr_{1-y}Fe_yO_3$ and $La_{1-x}Co_xCr_{1-y}Fe_yO_3$/r-GO, (a) The degradation-rate, (b) Linear-kinetic, (c) Rate-constant and (d) percentage degradation of dye.

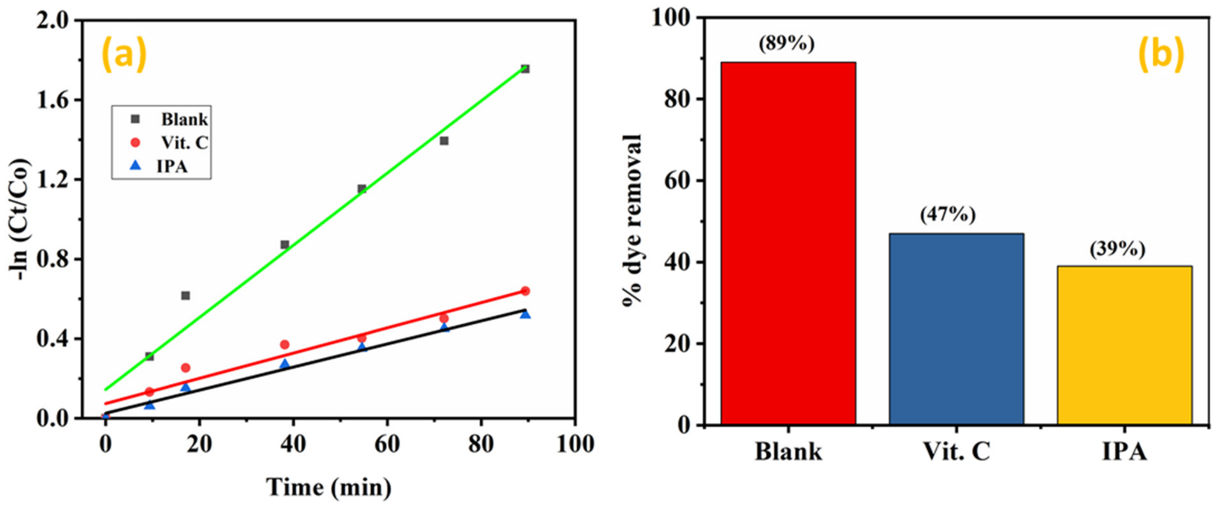

Fig. 9. (a) Photocatalytic degradation of CV over $La_{1-x}Co_xCr_{1-y}Fe_yO_3$/r-GO photo-catalyst alone and with different scavengers and (b) dye removal percentages in the presence of scavengers.

suppresses the electron/holes recombination process [73]. In comparison of PCA of fabricated photo-catalyst closely relates with reported studies (Table 2) and $La_{1-x}Co_xCr_{1-y}Fe_yO_3$/r-GO nanocomposite showed significant PCA versus reported related catalysts.

To confirm the species (OH• & •O2−) responsible for the degradation of dye, isopropyl alcohol (IPA) and ascorbic acid (Vit. C) were used for scavenging the OH• and •O2⁻, respectively, by keeping all other experimental conditions constant. The scavenger results are shown in Fig. 9a. The degradation efficiency of $La_{1-x}Co_xCr_{1-y}Fe_yO_3$-r-GO composite over CV dye, which declined in case of scavengers presence. Thus, the experimental results (Fig. 9b) infer that OH• and •O_2^- were the main species that were involved in the degradation of CV dye. The proposed mechanism of photo-catalyzed CV dye degradation is shown in reactions (Eqs. (14)–(22)) and the photocatalytic degradation mechanism is shown in Fig. 10.

$$La_{1-x}Co_xCr_{1-y}Fe_yO_3 + \text{Visible light} \rightarrow La_{1-x}Co_xCr_{1-y}Fe_yO_3\ (\bar{e}_{CB} + h^+{}_{VB}) \quad (14)$$

$$La_{1-x}Co_xCr_{1-y}Fe_yO_3(\bar{e}_{CB} + h^+{}_{VB}) + r\text{—}GO \rightarrow La_{1-x}Co_xCr_{1-y}Fe_yO_3\ (h^+{}_{VB}) + r\text{—}GO\ (\bar{e}) \quad (15)$$

$$La_{1-x}Co_xCr_{1-y}Fe_yO_3(h^+{}_{VB}) + H_2O \rightarrow OH^{\cdot} + H^+ \quad (16)$$

$$\bar{E}\ (r\text{—}GO) + O_2 \rightarrow r\text{—}GO + {}^{\cdot}O_2{}^{-\cdot} \quad (17)$$

$$^{\cdot}O_2{}^{-\cdot} + 2H^+ \rightarrow HO_2{}^{-\cdot} + H^+ \rightarrow 2OH^{\cdot} \quad (18)$$

$$^{\cdot}O_2{}^{-} + H_2O \rightarrow {}^{\cdot}OOH + HO_2{}^{-} \quad (19)$$

$$2^{\cdot}OOH \rightarrow O_2 + H_2O_2 \quad (20)$$

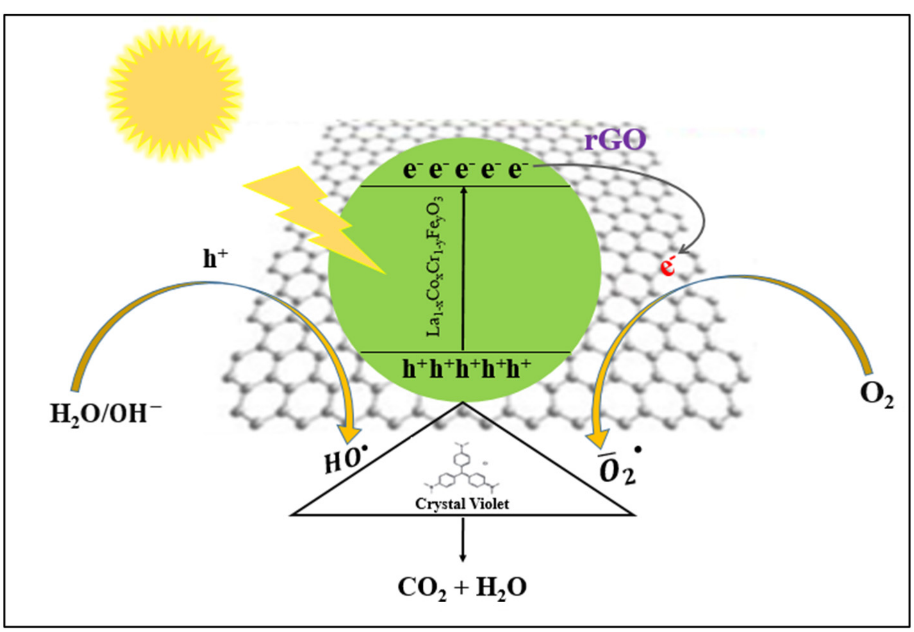

Fig. 10. Photocatalytic proposed mechanism for dye degradation over $La_{1-x}Co_xCr_{1-y}Fe_yO_3$/r-GO photocatalyst.

$$H_2O_2 + O_2^{-\cdot} \rightarrow OH^{\cdot} + HO^{-} + {}^{\cdot}O2^{-} \quad (21)$$

$$OH^{\cdot}/{}^{\cdot}O2^{-} + CV\ dye \rightarrow Degraded\ products \quad (22)$$

4. Conclusion

Pristine $LaCrO_3$, $La_{1\text{-}x}Co_xCr_{1\text{-}y}Fe_yO_3$ and $La_{1\text{-}x}Co_xCr_{1\text{-}y}Fe_yO_3$/r-GO nanocomposite were successfully fabricated via micro-emulsion and ultra-sonication method, respectively. The effect of Cr, Fe doping on $La_{1\text{-}x}Co_xCr_{1\text{-}y}Fe_yO_3$, and $La_{1\text{-}x}Co_xCr_{1\text{-}y}Fe_yO_3$/r-GO nanocomposite were studied, the electrical conductivity of the pristine $LaCrO_3$ was in the range of 2.17×10^{-2} Sm^{-1} to 7.4×10^{3} Sm^{-1}. Besides, the $La_{1\text{-}x}Co_xCr_{1\text{-}y}Fe_yO_3$/r-GO nanocomposite exhibited excellent PCA for CV dye degradation under visible light. The improved PCA of the $La_{1\text{-}x}Co_xCr_{1\text{-}y}Fe_yO_3$/r-GO composite is due to the surface area, low band gap and fast charge transportation character. In view of promising PCA of $La_{1\text{-}x}Co_xCr_{1\text{-}y}Fe_yO_3$/r-GO nanocomposite, it could be employed as a photocatalyst for the remediation of dyes in textile effluents.

Declaration of Competing Interest

The authors declare that they have no known competing financial interests or personal relationships that could have appeared to influence the work reported in this paper.

Acknowledgements

This research was funded by the Deanship of Scientific Research at Princess Nourah bint Abdulrahman University through the Fast-track Research Funding Program.

References

[1] M. Ahmad, I. Bhatti, K. Qureshi, N. Ahmad, J. Nisar, M. Zuber, A. Ashar, M. Khan, M. Iqbal, Graphene oxide supported $Fe_2(MoO_4)_3$ nano rods assembled round-ball fabrication via hydrothermal route and photocatalytic degradation of nonsteroidal anti-inflammatory drug, J. Mol. Liq. 301 (2020) 112343.
[2] K. Qureshi, M.Z. Ahmad, I.A. Bhatti, M. Zahid, J. Nisar, M. Iqbal, Graphene oxide decorated $ZnWO_4$ architecture synthesis, characterization and photocatalytic activity evaluation, J. Mol. Liq. 285 (2019) 778–789.
[3] S. Ata, A. Tabassum, I. Bibi, F. Majid, M. Sultan, S. Ghafoor, M.A. Bhatti, N. Qureshi, M. Iqbal, Lead remediation using smart materials. A review, Z. Phys. Chem. 233 (10) (2019) 1377–1409.
[4] U. Kamran, H.N. Bhatti, M. Iqbal, A. Nazir, Green synthesis of metal nanoparticles and their applications in different fields: a review, Z. Phys. Chem. 233 (9) (2019) 1325–1349.
[5] A.M. Awwad, M.W. Amer, M.M. Al-Aqarbeh, TiO_2-kaolinite nanocomposite prepared from the Jordanian kaolin clay: adsorption and thermodynamic of Pb(II) and Cd(II) ions in aqueous solution, Chem. Int. 6 (4) (2020) 168–178.
[6] A.M. Awwad, M.W. Amer, N.M. Salem, A.O. Abdeen, Green synthesis of zinc oxide nanoparticles (ZnO-NPs) using Ailanthus altissima fruit extracts and antibacterial activity, Chem. Int. 6 (3) (2020) 151–159.
[7] A.M. Awwad, N.M. Salem, M.M. Aqarbeh, F.M. Abdulaziz, Green synthesis, characterization of silver sulfide nanoparticles and antibacterial activity evaluation, Chem. Int. 6 (1) (2020) 42–48.
[8] S. Ajmal, I. Bibi, F. Majid, S. Ata, K. Kamran, K. Jilani, S. Nouren, S. Kamal, A. Ali, M. Iqbal, Effect of Fe and Bi doping on LaCoO3 structural, magnetic, electric and catalytic properties, J. Mater. Res. Technol. 8 (5) (2019) 4831–4842.
[9] I. Bibi, S. Hussain, F. Majid, S. Kamal, S. Ata, M. Sultan, M.I. Din, M. Iqbal, A. Nazir, Structural, dielectric and magnetic studies of perovskite [$Gd_{1-x}M_xCrO_3$ (M= La, Co, Bi)] nanoparticles: photocatalytic degradation of dyes, Z. Phys. Chem. 233 (10) (2019) 1431–1445.
[10] B.A. Josephine, A. Manikandan, V.M. Teresita, S.A. Antony, Fundamental study of $LaMg_xCr_{1-x}O_{3-\delta}$ perovskites nano-photocatalysts: sol-gel synthesis, characterization and humidity sensing, Korean J. Chem. Eng. 33 (5) (2016) 1590–1598.
[11] V.M. Teresita, A. Manikandan, B.A. Josephine, S. Sujatha, S.A. Antony, Electromagnetic properties and humidity-sensing studies of magnetically recoverable $LaMg_xFe_{1-x}O_{3-\delta}$ perovskites nano-photocatalysts by sol-gel route, J. Superconduct. Novel Magnet. 29 (6) (2016) 1691–1701.
[12] S. Hussain, M.S. Javed, N. Ullah, A. Shaheen, N. Aslam, I. Ashraf, Y. Abbas, M. Wang, G. Liu, G. Qiao, Unique hierarchical mesoporous $LaCrO_3$ perovskite oxides for highly efficient electrochemical energy storage applications, Ceram. Int. 45 (12) (2019) 15164–15170.
[13] M. Enhessari, A. Salehabadi, A. Khoobi, R. Amiri, Kinetic properties and structural analysis of $LaCrO_3$ nanoparticles, Mater. Sci. Poland 35 (2) (2017) 368–373.
[14] J. Fergus, Metallic interconnects for solid oxide fuel cells, Mater. Sci. Eng. A 397 (2005) 271–283.
[15] G. Saracco, G. Scibilia, A. Iannibello, G. Baldi, Methane combustion on Mg-doped $LaCrO_3$ perovskite catalysts, Appl. Catal. B 8 (2) (1996) 229–244.
[16] S. Iqbal, I. Bibi, S. Ata, S. Kamal, S.M. Ibrahim, M. Iqbal, Gd and Co-substituted $LaNiO_3$ and their nanocomposites with r-GO for photocatalytic applications, Diam. Relat. Mater. 110 (2020) 108119.
[17] M. Arshad, A. Qayyum, G.A. Shar, G.A. Soomro, A. Nazir, B. Munir, M. Iqbal, Zn-doped SiO_2 nanoparticles preparation and characterization under the effect of various solvents: antibacterial, antifungal and photocatlytic performance evaluation, J. Photochem. Photobiol. B 185 (2018) 176–183.
[18] I. Bibi, U. Ali, S. Kamal, S. Ata, S.M. Ibrahim, F. Majid, Z. Nazeer, F. Rehman, S. Iqbal, M. Iqbal, Synthesis of $La_{1\text{-}x}Co_xFe_{1\text{-}y}Cr_yO_3$ nano crystallites for enhanced ferroelectric, magnetic and photocatalytic properties, J. Mater. Res. Technol. 9 (6) (2020) 12031–12042.
[19] S. Ata, I. Shaheen, A. Qurat ul, S. Ghafoor, M. Sultan, F. Majid, I. Bibi, M. Iqbal, Graphene and silver decorated ZnO composite synthesis, characterization and photocatalytic activity evaluation, Diam. Relat. Mater. 90 (2018) 26–31.
[20] M. Abbas, M. Adil, S. Ehtisham-ul-Haque, B. Munir, M. Yameen, A. Ghaffar, G.A. Shar, M. Asif Tahir, M. Iqbal, *Vibrio fischeri* bioluminescence inhibition assay for ecotoxicity assessment: a review, Sci. Total Environ. 626 (2018) 1295–1309.
[21] M. Iqbal, Vicia faba bioassay for environmental toxicity monitoring: a review, Chemosphere 144 (2016) 785–802.
[22] M. Iqbal, M. Abbas, A. Nazir, A.Z. Qamar, Bioassays based on higher plants as excellent dosimeters for ecotoxicity monitoring: a review, Chem. Int. 5 (1) (2019) 1–80.
[23] R. Arshad, T.H. Bokhari, K.K. Khosa, I.A. Bhatti, M. Munir, M. Iqbal, D.N. Iqbal, M.I. Khan, M. Iqbal, A. Nazir, Gamma radiation induced degradation of anthraquinone reactive Blue-19 dye using hydrogen peroxide as oxidizing agent, Rad. Phys. Chem. 168 (2020) 108637.
[24] U.H. Siddiqua, S. Ali, M. Iqbal, T. Hussain, Relationship between structure and dyeing properties of reactive dyes for cotton dyeing, J. Mol. Liq. 241 (2017) 839–844.
[25] M. Arshad, A. Qayyum, G. Abbas, R. Haider, M. Iqbal, A. Nazir, Influence of different solvents on portrayal and photocatalytic activity of tin-doped zinc oxide nanoparticles, J. Mol. Liq. 260 (2018) 272–278.
[26] A. Ayach, S. Fakhi, Z. Faiz, A. Bouih, O. Ait malek Benkdad, M. Benmansour, A. Laissaoui, M. Adjour, Y. Elbatal, I. Vioque, G. Manjon, Adsorption of methylene blue on bituminous schists from Tarfaya-Boujdour, Chem. Int. 3 (4) (2017) 442–451.
[27] A. Babarinde, G.O. Onyiaocha, Equilibrium sorption of divalent metal ions onto groundnut (Arachis hypogaea) shell: kinetics, isotherm and thermodynamics, Chem. Int. 2 (3) (2016) 37–46.
[28] N. Benabdallah, D. Harrache, A. Mir, M. De La Guardia, F. Benhachem, Bioaccumulation of trace metals by red alga *Corallina elongata* in the coast of Beni Saf, west coast, Algeria, Chem. Int. 3 (3) (2017) 220–231.
[29] K.B. Daij, S. Bellebia, Z. Bengharez, Comparative experimental study on the COD removal in aqueous solution of pesticides by the electrocoagulation process using monopolar iron electrodes, Chem. Int. 3 (4) (2017) 420–427.
[30] K. Djehaf, A.Z. Bouyakoub, R. Ouhib, H. Benmansour, A. Bentouaf, A. Mahdad, N. Moulay, D. Bensaid, M. Ameri, Textile wastewater in Tlemcen (Western Algeria): impact, treatment by combined process, Chem. Int. 3 (4) (2017) 414–419.
[31] K. Legrouri, E. Khouya, H. Hannache, M. El Hartti, M. Ezzine, R. Naslain, Activated carbon from molasses efficiency for Cr(VI), Pb(II) and Cu(II) adsorption: a mechanistic study, Chem. Int. 3 (3) (2017) 301–310.
[32] F. Minas, B.S. Chandravanshi, S. Leta, Chemical precipitation method for chromium removal and its recovery from tannery wastewater in Ethiopia, Chem. Int. 3 (4) (2017) 392–405.
[33] L. Bulgariu, L.B. Escudero, O.S. Bello, M. Iqbal, J. Nisar, K.A. Adegoke, F. Alakhras, M. Kornaros, I. Anastopoulos, The utilization of leaf-based adsorbents for dyes removal: a review, J. Mol. Liq. 276 (2019) 728–747.
[34] A. Kausar, G. MacKinnon, A. Alharthi, J. Hargreaves, H.N. Bhatti, M. Iqbal, A green approach for the removal of Sr(II) from aqueous media: kinetics, isotherms and thermodynamic studies, J. Mol. Liq. 257 (2018) 164–172.
[35] A. Kausar, M. Iqbal, A. Javed, K. Aftab, Z.-i.-H. Nazli, H.N. Bhatti, S. Nouren, Dyes adsorption using clay and modified clay: a review, J. Mol. Liq. 256 (2018) 395–407.
[36] M. Palutoglu, B. Akgul, V. Suyarko, M. Yakovenko, N. Kryuchenko, A. Sasmaz, Phytoremediation of cadmium by native plants grown on mining soil, Bull. Environ. Contam. Toxicol. 100 (2) (2018) 293–297.
[37] M. Sasmaz, E. Obek, A. Sasmaz, Bioaccumulation of uranium and thorium by Lemna minor and Lemna gibba in Pb-Zn-Ag tailing water, Bull. Environ. Contam. Toxicol. 97 (6) (2016) 832–837.
[38] K. Qureshi, M. Ahmad, I. Bhatti, M. Iqbal, A. Khan, Cytotoxicity reduction of wastewater treated by advanced oxidation process, Chem. Int. 1 (53) (2015) 59.
[39] M.A. Jamal, M. Muneer, M. Iqbal, Photo-degradation of monoazo dye blue 13 using advanced oxidation process, Chem. Int. 1 (1) (2015) 12–16.
[40] M. Aadil, W. Shaheen, M.F. Warsi, M. Shahid, M.A. Khan, Z. Ali, S. Haider, I. Shakir, Superior electrochemical activity of α-Fe_2O_3/rGO nanocomposite for advance energy storage devices, J. Alloy. Comp. 689 (2016) 648–654.
[41] M. Aadil, S. Zulfiqar, H. Sabeeh, M.F. Warsi, M. Shahid, I.A. Alsafari, I. Shakir, Enhanced electrochemical energy storage properties of carbon coated Co_3O_4 nanoparticles-reduced graphene oxide ternary nano-hybrids, Ceram. Int. 46 (11, Part A) (2020) 17836–17845.
[42] A. Rahman, M. Aadil, M. Akhtar, M.F. Warsi, A. Jamil, I. Shakir, M. Shahid, Magnetically recyclable $Ni_{1\text{-}x}Cd_xCe_yFe_{2\text{-}y}O_4$-rGO nanocomposite photocatalyst for visible light driven photocatalysis, Ceram. Int. 46 (2020) 13517–13526.

[43] S. Munir, A. Rasheed, S. Zulfiqar, M. Aadil, P.O. Agboola, I. Shakir, M.F. Warsi, Synthesis, characterization and photocatalytic parameters investigation of a new $CuFe_2O_4$/Bi_2O_3 nanocomposite, Ceram. Int. 46 (2020) 29182–29190.
[44] R. Wang, K. Shi, D. Huang, J. Zhang, S. An, Synthesis and degradation kinetics of TiO_2/GO composites with highly efficient activity for adsorption and photocatalytic degradation of MB, Sci. Report. 9 (1) (2019) 18744.
[45] A.A. Shah, S. Ahmad, A. Azam, Investigation of structural, optical, dielectric and magnetic properties of $LaNiO_3$ and $LaNi_{1-x}M_xO_3$ (M= Fe, Cr & co; x= 5%) nanoparticles, J. Magnet. Magnet. Mater. 494 (2020) 165812.
[46] W. Rativa-Parada, J. Gómez-Cuaspud, E. Vera, J. Carda, Structural and electrical study of $LaCrO_3$ modified with Fe and co, J. Phys. Conf. Ser. 786 (2017), 012029, .
[47] K. Zafar, M. Aadil, M.N. Shahi, H. Sabeeh, M.F. Nazar, M. Iqbal, M.A. Yousuf, Physical, structural and dielectric parameters evaluation of new $Mg_{1-x}Co_xNi_yFe_{2-y}O_4$ nanoferrites synthesized via wet chemical approach, Energy Mater. 1 (1) (2020) 36–44.
[48] O.B. Pavlovska, L.O. Vasylechko, I.V. Lutsyuk, N.M. Koval, Y.A. Zhydachevskii, A. Pieniążek, Structure peculiarities of micro- and nanocrystalline perovskite ferrites $La_{1-x}Sm_xFeO_3$, Nanoscale Res. Lett. 12 (1) (2017) 153.
[49] Q. Choudhry, M. Azhar Khan, G. Nasar, A. Mahmood, M. Shahid, I. Shakir, M. Farooq Warsi, Synthesis, characterization and study of magnetic, electrical and dielectric properties of $La_{1-x}Dy_xCo_{1-y}Fe_yO_3$ nanoparticles prepared by wet chemical route, J. Magnet. Magnet. Mater. 393 (2015) 67–72.
[50] A.A. Shah, S. Ahmad, A. Azam, Investigation of structural, optical, dielectric and magnetic properties of $LaNiO_3$ and $LaNi_{1-x}M_xO_3$ (M = Fe, Cr & co; x = 5%) nanoparticles, J. Magnet. Magnet. Mater. 494 (2020) 165812.
[51] M. Bradha, S. Hussain, S. Chakravarty, G. Amarendra, A. Ashok, Synthesis, structure and total conductivity of A-site doped $LaTiO_{3-\delta}$ perovskites, J. Alloy. Comp. 626 (2015) 245–251.
[52] S. Ajami, Y. Mortazavi, A. Khodadadi, F. Pourfayaz, S. Mohajerzadeh, Highly selective sensor to CH_4 in presence of CO and ethanol using $LaCoO_3$ perovskite filter with Pt/SnO_2, Sens. Actuat. B 117 (2) (2006) 420–425.
[53] M. Ghasdi, H. Alamdari, S. Royer, A. Adnot, Electrical and CO gas sensing properties of nanostructured $La_{1-x}Ce_xCoO_3$ perovskite prepared by activated reactive synthesis, Sens. Actuat. B 156 (2011) 147–155.
[54] D. Meziani, A. Reziga, G. Rekhila, B. Bellal, M. Trari, Hydrogen evolution under visible light over $LaCoO_3$ prepared by chemical route, Energy Conver. Manage. 82 (2014) 244–249.
[55] K. Nalwa, A. Garg, Phase evolution, magnetic and electrical properties in Sm-doped bismuth ferrite, J. Appl. Phys. 103 (2008) 044101.
[56] Z. Anwar, M. Khan, A. Mahmood, M. Asghar, I. Shakir, M. Shahid, I. Bibi, M. Warsi, $Tb_xBi_{1-x}FeO_3$ nanoparticulate multiferroics fabricated by micro-emulsion technique: structural elucidation and magnetic behavior evaluation, J. Magnet. Magnet. Mater. 355 (2014) 169–172.
[57] Y. Luo, X. Liu, X. Li, Electrical properties of $BaTiO_3$-based NTC thermistors doped by $BaBiO_3$ and La_2O_3, J. Mater. Sci. Mater. Electron. 17 (2006) 909–913.
[58] M. Sukumar, L. Kennedy, J. Vijaya, B. Al-Najar, M. Bououdina, Facile microwave assisted combustion synthesis, structural, optical and magnetic properties of $La_{2-x}Sr_xCuO_4$ (0 ≤ x ≤ 0.5) perovskite nanostructures, J. Magnet. Magnet. Mater. 465 (2018) 48–57.
[59] L. Tepech-Carrillo, A. Escobedo-Morales, A. Pérez-Centeno, E. Chigo-Anota, J. Sánchez-Ramírez, E. López-Apreza, J. Gutiérrez-Gutiérrez, Preparation of nanosized $LaCoO_3$ through calcination of a hydrothermally synthesized precursor, J. Nanomater. 2016 (2016) 6917950.
[60] K.D. Singh, R. Pandit, R. Kumar, Effect of rare earth ions on structural and optical properties of specific perovskite orthochromates; $RCrO_3$ (R= La, Nd, Eu, Gd, Dy, and Y), Solid Stat. Sci. 85 (2018) 70–75.
[61] V.D. Nithya, R. Jacob Immanuel, S.T. Senthilkumar, C. Sanjeeviraja, I. Perelshtein, D. Zitoun, R. Kalai Selvan, Studies on the structural, electrical and magnetic properties of $LaCrO_3$, $LaCr0_5Cu0_5O_3$ and $LaCr0_5Fe0_5O_3$ by sol–gel method, Mater. Res. Bull. 47 (8) (2012) 1861–1868.
[62] O. Polat, Z. Durmus, F.M. Coskun, M. Coskun, A. Turut, Engineering the band gap of $LaCrO_3$ doping with transition metals (Co, Pd, and Ir), J. Mater. Sci. 53 (5) (2018) 3544–3556.
[63] F. Lahcen, A. Mahmoud, F. Boschini, M. Hamedoun, A. Benyoussef, M. Ait Ali, O. Mounkachi, Structural, magnetic, and magnetocaloric properties in rare earth orthochromite (Sm, Nd, and La)CrO_3 for cooling product, J. Superconduct. Novel Magnet. 33 (2019) 1023–1030.
[64] Y. Wan, J. Yang, H. Hou, S. Xu, G. Liu, S. Hussain, G. Qiao, Synthesis and microstructures of $La_{1-x}Ca_xCrO_3$ perovskite powders for optical properties, J. Mater. Sci. Mater. Electron. 30 (4) (2019) 3472–3481.
[65] V.S. Shinde, K.H. Kapadnis, C.P. Sawant, P.B. Koli, R.P. Patil, Screen print fabricated In^{3+} decorated perovskite lanthanum chromium oxide ($LaCrO_3$) thick film sensors for selective detection of volatile petrol vapors, J. Inorgan. Organometal. Polym. Mater. (2020) 1–15 Ahead of print.
[66] M.F. Warsi, B. Bashir, S. Zulfiqar, M. Aadil, M.U. Khalid, P.O. Agboola, I. Shakir, M.A. Yousuf, M. Shahid, $Mn_{1-x}Cu_xO_2$/reduced graphene oxide nanocomposites: synthesis, characterization, and evaluation of light mediated catalytic studies, Ceram. Int. (2020) https://doi.org/10.1016/j.ceramint.2020.10.082.
[67] G. Xiao, J. Ning, Z. Liu, Y. Sui, Y. Wang, Q. Dong, W. Tian, B. Liu, G. Zou, B. Zou, Solution synthesis of copper selenide nanocrystals and their electrical transport properties, CrystEngComm 14 (2012) 2139–2144.
[68] D. Suresh, An Investigation on the Band Gap and Band Edge of Semi-conducting Lanthanum Transition Metal Perovskites for Photocatalytic Applications, MS thesis https://scholarcommons.usf.edu/etd/5779/ 2015.
[69] R. Suresh, R. Udayabhaskar, C. Sandoval, E. Ramírez, R.V. Mangalaraja, H.D. Mansilla, D. Contreras, J. Yáñez, Effect of reduced graphene oxide on the structural, optical, adsorption and photocatalytic properties of iron oxide nanoparticles, New J. Chem. 42 (11) (2018) 8485–8493.
[70] B. Bashir, M.U. Khalid, M. Aadil, S. Zulfiqar, M.F. Warsi, P.O. Agboola, I. Shakir, $Cu_xNi_{1-x}O$ nanostructures and their nanocomposites with reduced graphene oxide: synthesis, characterization, and photocatalytic applications, Ceram. Int. (2020) https://doi.org/10.1016/j.ceramint.2020.09.209.
[71] A. Rahman, M. Aadil, M. Akhtar, M.F. Warsi, A. Jamil, I. Shakir, M. Shahid, Magnetically recyclable Ni1-xCdxCeyFe2-yO4-rGO nanocomposite photocatalyst for visible light driven photocatalysis, Ceram. Int. 46 (9) (2020) 13517–13526.
[72] T. Chhabra, A. Kumar, A. Bahuguna, V. Krishnan, Reduced graphene oxide supported MnO_2 nanorods as recyclable and efficient adsorptive photocatalysts for pollutants removal, Vacuum 160 (2019) 333–346.
[73] W. Ruan, J. Hu, J. Qi, Y. Hou, R. Cao, X. Wei, Removal of crystal violet by using reduced-graphene-oxide-supported bimetallic Fe/Ni nanoparticles (rGO/Fe/Ni): application of artificial intelligence modeling for the optimization process, Materials (Basel) 11 (5) (2018) 865.
[74] Y. Xue, Q. Chang, X. Hu, J. Cai, H. Yang, A simple strategy for selective photocatalysis degradation of organic dyes through selective adsorption enrichment by using a complex film of CdS and carboxylmethyl starch, J. Environ. Manag. 274 (2020) 111184.
[75] V.T. Le, V.D. Doan, T.T.N. Le, M.U. Dao, T.-T.T. Vo, H.H. Do, D.Q. Viet, V.A. Tran, Efficient photocatalytic degradation of crystal violet under natural sunlight using Fe_3O_4/ZnO nanoparticles embedded carboxylate-rich carbon, Mater. Lett. 283 (2021) 128749.
[76] Y. Panahian, N. Arsalani, R. Nasiri, Enhanced photo and sono-photo degradation of crystal violet dye in aqueous solution by 3D flower like F-TiO_2(B)/fullerene under visible light, J. Photochem. Photobiol. A 365 (2018) 45–51.
[77] R.S. Saravan, M. Muthukumaran, S.M. Mubashera, M. Abinaya, P.V. Prasath, R. Parthiban, F. Mohammad, W.C. Oh, S. Sagadevan, Evaluation of the photocatalytic efficiency of cobalt oxide nanoparticles towards the degradation of crystal violet and methylene violet dyes, Optik 207 (2020) 164428.
[78] R. Ullah, C. Liu, H. Panezai, A. Gul, J. Sun, X. Wu, Controlled crystal phase and particle size of loaded-TiO2 using clinoptilolite as support via hydrothermal method for degradation of crystal violet dye in aqueous solution, Arab. J. Chem. 13 (2) (2020) 4092–4101.
[79] S. Sathiyavimal, S. Vasantharaj, M. Shanmugavel, E. Manikandan, P. Nguyen-Tri, K. Brindhadevi, A. Pugazhendhi, Facile synthesis and characterization of hydroxyapatite from fish bones: Photocatalytic degradation of industrial dyes (crystal violet and Congo red), Prog. Organ. Coat. 148 (2020) 105890.
[80] R. Rahimi, M. Moshari, M. Rabbani, Photocatalytic Degredration of Methylene Blue and Crystal Violet by Sulfur/Reduced Graphene Oxide Composite, https://sciforum.net/manuscripts/2544/manuscript.pdf 2014.